Observation of Topological Berry Phases with a Single Phonon in an Ion Microtrap Array

Justin F. Niedermeyer,[1,2,*] Nathan K. Lysne,[1,2,†] Katherine C. McCormick,[1,2] Jonas Keller,[1,2,‡] Craig W. Hogle,[3] Matthew G. Blain,[3] Edwin J. Heller,[3] Roman Schmied,[4,§] Robert Jördens,[1,‖] Susanna L. Todaro,[1,2] David J. Wineland,[1,¶] Andrew C. Wilson,[1] Daniel H. Slichter,[1] and Dietrich Leibfried[1,**]

[1]*National Institute of Standards and Technology, Boulder, Colorado 80305, USA*
[2]*Department of Physics, University of Colorado Boulder, Boulder, Colorado 80309, USA*
[3]*Sandia National Laboratories, Albuquerque, New Mexico 87123, USA*
[4]*Department of Physics, University of Basel, CH-4056 Basel, Switzerland*

(Received 31 March 2026; accepted 2 October 2026; published 10 November 2026)

Controlled quantum mechanical motion of trapped atomic ions can be used to simulate and explore collective quantum phenomena and to process quantum information. Groups of cold atomic ions confined in an externally applied trapping potential self-organize into "Coulomb crystals" due to their mutual electrostatic repulsion. The motion of the ions in these crystals is strongly coupled, and most eigenmodes of motion involve multiple ions. While this enables studies of many-body physics, it limits the flexibility and tunability of the system as a quantum platform. Here, we demonstrate an array of trapped ions in individual trapping sites whose motional modes can be controllably coupled and decoupled by locally tuning the confining potential for each ion. A single motional quantum, or phonon, can be coherently shared among two or three ions located at the vertices of an equilateral triangle 30 μm on a side. We tune the motional eigenmodes about closed contours in configuration space and observe that, if the contour adiabatically encircles a conical intersection present in the motional eigenvalue surfaces, the single-phonon wave function acquires a topological Berry phase that is independent of the contour shape. We characterize these phases by single-phonon interference and study how phase changes occur when the motional mode tuning becomes nonadiabatic. Our results show that precise, individual quantum control of ion motion in a two-dimensional array provides unique access to quantum multibody effects.

DOI: 10.1103/td5k-t1mf

Subject Areas: Atomic and Molecular Physics, Quantum Physics

I. INTRODUCTION

The quantized, shared motion of trapped ions is essential to their use for quantum simulation [1,2], quantum information processing [3], and quantum logic spectroscopy [4–6]. Much of the work in these applications uses traps that create approximately harmonic potentials with a single minimum. Depending on the number of ions and the geometry of the trapping potential, the ions self-organize around this minimum in one-dimensional strings [7] or higher-dimensional arrangements [8–15]. External fields are then applied to control the interactions of the ions bound in that potential by driving their modes of motion; such systems have been used to perform a variety of quantum simulations [16–20]. In two dimensions (2D), and for sufficiently large numbers of ions, triangular lattices are typically formed in the crystal centers [14,16]. Such 2D Coulomb and Wigner crystals composed of hundreds of trapped ions have enabled simulations of spin models with tunable, patterned, long-range interactions [15–17]. Lattice defects in such systems arising from a variety of technical sources can produce many different metastable crystal configurations that are not necessarily at the lowest energy but are stable over long timescales [14]. This hard-to-control variation in larger self-organized crystals leads to corresponding variation in the ion-ion interactions. Precise

*Contact author: justin.f.niedermeyer@gmail.com
†Present address: Quantinuum K.K., Chiyoda-ku, Tokyo, 100-0004, Japan.
‡Present address: Physikalisch-Technische Bundesanstalt, D-38116 Braunschweig, Germany.
§Present address: Viewpointsystem GmbH, A-1010 Vienna, Austria.
‖Present address: QUARTIQ GmbH, D-12489 Berlin, Germany.
¶Present address: Department of Physics, University of Oregon, Eugene, Oregon 97403-1274, USA.
**Contact author: dietrich.leibfried@nist.gov

Published by the American Physical Society under the terms of the Creative Commons Attribution 4.0 International license. Further distribution of this work must maintain attribution to the author(s) and the published article's title, journal citation, and DOI.

control over couplings between ion pairs is further complicated by unequal participation of the ions in most of the motional modes, posing a substantial challenge for tuning interaction strengths as the number of ions increases.

In principle, arbitrary 2D geometries of ions, including regular lattices, quasiperiodic tilings, non-Euclidean lattices [21], and tunable defects or dislocations, can be realized by trapping ions individually in a set of separate, independently controllable potential wells in a microtrap array [22,23]. Such arrangements can create inherent symmetries and topological features of dynamically tunable ion interactions not accessible to self-organized ion crystals that occupy a single potential well. To observe coherent interactions, the wells need to be close enough to each other that the Coulomb coupling rate is substantially larger than all motional decoherence rates in the system. Previous demonstrations of microtrap arrays have shown the ability to load and deterministically rearrange ions among wells [24,25], but the creation of individually controllable wells requires electrodes in close proximity to the ions, such that the motional heating rates were equal to or larger than the motional coupling rate between wells [26,27].

Here, we demonstrate quantum-coherent motional coupling and the direct quantitative observation of topological Berry phases [28] in a fully tunable 2D microtrap array consisting of three ions arranged in an equilateral triangle (Fig. 1). We prepare all nine modes of motion close to their ground states and inject a single phonon to create an entangled Bell state of the coupled eigenmodes of the form $(1/\sqrt{2})(|1\rangle_{e1}|0\rangle_{e2} + e^{i\Delta\omega t}|0\rangle_{e1}|1\rangle_{e2})$, where the kets indicate zero- and one-phonon-number states of eigenmodes $e1$ and $e2$ and $\Delta\omega$ their frequency difference (see below for more details). By dynamically tuning the couplings between motional modes, we can continuously deform the character of the single-phonon motional state to encircle a conical intersection of the motional eigenvalue surfaces with a variety of different paths traversed at different rates. We can isolate and determine the resulting topological Berry phases [28] with high contrast and approximately 1% relative uncertainty in single-phonon interference experiments. While conical intersections [29] (also known as diabolical points and closely related to Dirac cones [30]) have profound physical implications, for example, in molecules involved in photosynthesis [31] and two-dimensional materials such as graphene [32], to the best of our knowledge, only the Berry flux around Dirac cones has previously been quantitatively determined with approximately 10% uncertainty by Aharonov-Bohm interferometry in momentum space with cold atoms in a hexagonal optical lattice [33]. In addition to a precise determination of Berry phases, we also demonstrate their independence from the shape of the path and its number of turns away from the conical intersection in the adiabatic limit. We then decrease the duration of traversing a certain path, quantitatively study the phase when adiabaticity breaks down, and find good agreement with numerical solutions of the full Schrödinger equation. Other related prior experiments using quantum simulators have observed dynamics near conical intersections including wave-packet branching [34] and geometric-phase signatures in measured or reconstructed motional distributions [35,36].

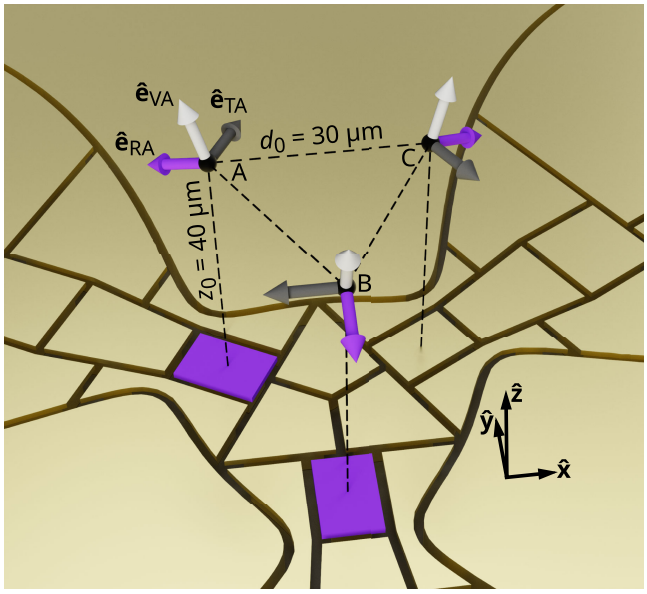


FIG. 1. Rendering of the triangular 2D ion microtrap array. Electrodes are shown in gold and gaps in black. Black spheres labeled A, B, and C mark the positions of the potential wells where $^9Be^+$ ions are trapped. Colored arrows [labeled $\hat{\mathbf{e}}_{RA}$ (purple), $\hat{\mathbf{e}}_{VA}$, (white), and $\hat{\mathbf{e}}_{TA}$ (gray) in site A] indicate the radial, vertical, and tangential principal axis directions, respectively, in all three sites. The electrodes closest to site A and site B, shown in purple, are used to fine-tune the site curvatures (second-order derivatives at the site potential minimum).

II. COUPLED TRIANGLE ARRAY

We now turn to the theory of coupled motional modes for an array of three potential wells, considering here the specific case of an equilateral triangle as illustrated in Fig. 1 with the three sites labeled A, B, and C. The three trapping sites host three sets of nearly equal potential curvatures (second spatial derivatives of the applied trapping potential) along corresponding principal axes $\hat{\mathbf{e}}_{RX}$, $\hat{\mathbf{e}}_{TX}$, and $\hat{\mathbf{e}}_{VX}$ $(X = A, B, C)$ in each site, respectively (shown in Fig. 1 and labeled for site A). The principal axes with the smallest potential curvatures point along the R directions and provide the strongest interion couplings. All experiments described here are performed on the modes along the R directions. All physical details of the ions, the trap, and the Coulomb interactions can be represented by three unitless 3-by-3 matrices and five quantities that fully specify the curvature matrix (Hessian) $\mathbf{H}$ and determine the eigenvalues and eigenvectors of the coupled ion motion (see Appendix A for more details). In the basis of the

uncoupled oscillators with products of number states $|klm\rangle_{ABC} = |k\rangle_A|l\rangle_B|m\rangle_C$, the Hessian is given by

$$\mathbf{H} = k_{\text{offs}}\begin{pmatrix}1&0&0\\0&1&0\\0&0&1\end{pmatrix} + \Delta k\begin{pmatrix}1&1&1\\1&1&1\\1&1&1\end{pmatrix} + \Delta k\begin{pmatrix}s_A+\alpha s_B & 0 & 0\\ 0 & s_B+\alpha s_A & 0\\ 0 & 0 & \alpha(s_A+s_B)\end{pmatrix}. \quad (1)$$

The curvature k_{offs} expresses equal curvature of the site potentials along the set of principal axes ($\hat{\mathbf{e}}_{RA}$, $\hat{\mathbf{e}}_{RB}$, and $\hat{\mathbf{e}}_{RC}$, shown with purple arrows in Fig. 1). It multiplies the identity matrix, and, consequently, any three-component vector is an eigenvector of this part with eigenvalue k_{offs} that offsets the eigenvalues of the remainder of $\mathbf{H}$. The curvature Δk characterizes the Coulomb interaction and multiplies the interaction matrix with all elements equal to one, which reflects the triangular symmetry of the system that renders the Coulomb interaction between any pair of ions identical. In our implementation, $k_{\text{offs}} \gg \Delta k > 0$ and the interaction matrix has one eigenvalue $\delta k_3 = 3\Delta k$ with eigenvector $\mathbf{c}^{(3)} = (c_A^{(3)}, c_B^{(3)}, c_C^{(3)})^T = 1/\sqrt{3}(1,1,1)^T$ and eigenvalues $\delta k_{1,2} = 0$ for any two vectors that are mutually orthogonal and orthogonal to $\mathbf{c}^{(3)}$. One choice is $\mathbf{c}^{(1)} = 1/\sqrt{2}(0,1,-1)^T$, $\mathbf{c}^{(2)} = 1/\sqrt{6}(2,-1,-1)^T$. The unitless quantities s_A and s_B describe tuning factors added to the site curvatures that we can realize by applying suitable potentials to the electrodes closest to the sites labeled A and B, respectively, shown in purple in Fig. 1. The effect of these electrodes on the two adjacent sites leads to equal curvature changes proportional to s_A and s_B, respectively, expressed by the proportionality factor α. The ion in site A does not participate in eigenmode $\mathbf{c}^{(1)}$. While $s_B = 0$, $\mathbf{c}^{(1)}$ remains an eigenvector of $\mathbf{H}$ for $s_A \neq 0$ with an eigenvalue $k_{\text{offs}} + \Delta k\,\alpha\, s_A$ that is linear in s_A.

The normalized differences $\delta k_j/\Delta k$ of the eigenvalues of $\mathbf{H}$ from k_{offs} as a function of general s_A and s_B are shown in Fig. 2(a). Two of the eigenvalue surfaces (shown in red and blue) meet in a conical intersection at $s_A = s_B = 0$ with coalescing eigenvalues k_{offs}, while the third surface (green) maintains a substantial gap $\geq 3\Delta k$ to the other two surfaces. The conical intersection is a consequence of the symmetry of the array. When all tuning parameters are set to zero, the threefold symmetry of the array enforces that the pairwise coupling between the ions is identical and described by the middle matrix (multiplied by Δk) in Eq. (1). All three rows of this matrix are identical, and, as a consequence, the matrix has a two-dimensional null space, two orthogonal nonzero eigenvectors with coalescing eigenvalues of zero. We can prepare an eigenstate or a superposition of eigenstates of the motion and then tune the local curvatures, and thereby the Hamiltonian of the coupled ion motion, by changing s_A and s_B. If this tuning is sufficiently slow, the adiabatic theorem applies and initial eigenstates of the coupled motion remain eigenstates throughout. Eigenstates such as those with eigenvalues on the lower two surfaces acquire a topological (or Berry)

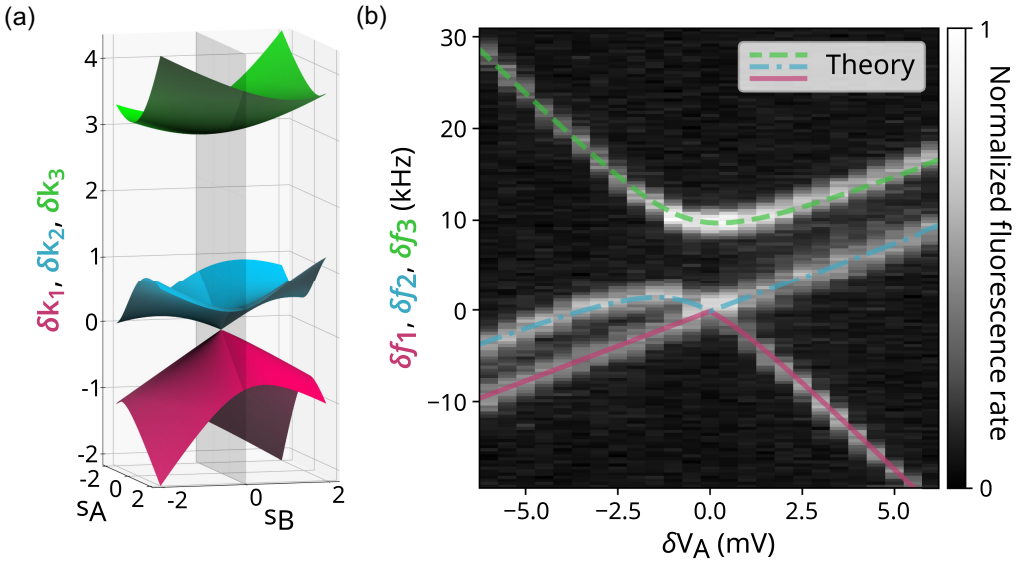


FIG. 2. (a) Radial motion eigenvalue surfaces vs tuning parameters s_A and s_B. The lower two manifolds (blue and red) form a conical intersection at $s_A = s_B = 0$. The semitransparent gray plane indicates a cut through the surfaces along $s_B = 0$ where the eigenmode frequencies [related to the curvature eigenvalues by $\delta f_j = (1/2\pi)\delta k_j/(2m\omega_R)$] were experimentally measured, with data shown in (b). The observed normalized fluorescence rate is shown as a function of the curvature tuning voltage δV_A and the difference δf between the excitation frequency and the eigenfrequencies at the conical intersection $\omega_R/(2\pi)$. The colored lines are the best fit to theory with eigenfrequencies colored in analogy to (a).

phase of π when s_A and s_B are adiabatically tuned along a closed path that encloses the conical intersection at $s_A = s_B = 0$ [28]. If the conical intersection is not enclosed, for example, if the initial state is an eigenstate with eigenvalue on the top surface (green), or if a path on the lower two surfaces does not enclose the conical intersection, the Berry phase is zero. The Berry phase acquired in either case is independent of the shape of the path and the duration required to move through it as long as the process remains sufficiently adiabatic.

III. THE TRIANGULAR ION MICROTRAP ARRAY

A view of the 2D ion microtrap array is shown in Fig. 1. The confining potential is produced by a single rf electrode with a hexagonal outer shape and a "cloverleaf"-shaped cutout with threefold symmetry that is segmented into 30 control electrodes (see Refs. [37,38] for overviews of all electrodes). The trap is microfabricated in a multilayer process with a top electrode layer made of aluminum coated with evaporated gold and buried electrical routing layers. Gaps in the electrodes are approximately as wide as the metal thickness (approximately 1.4 μm), and the insulating dielectric (SiO_2) below the electrodes is hidden from line of sight to ion positions. The metal layer (not shown) immediately below the electrode (top metal) layer is grounded in the electrode gap regions [39]. We apply a potential to the rf electrode with an amplitude of approximately 42 V oscillating at approximately 121.1 MHz to create three potential wells on the corners A, B, and C of an equilateral triangle with side length $d_0 = 30$ μm that are $z_0 = 40$ μm from the electrode surface. We trap a single $^9Be^+$ ion in each potential well.

By applying linear combinations of voltages to the 30 control electrodes, we can tune the electric field vector at the position of a given ion without affecting the curvature tensor (and vice versa) and without appreciably changing the curvatures or fields at the positions of the other two ions. Site-specific applied electric fields can be used to compensate stray electric fields and minimize ion micromotion [40] or for individual addressing [37]. Site-specific curvature tuning is used to compensate for stray curvatures and to adjust the principal axis orientations and confinement strengths in each well. More information on these procedures can be found in Ref. [38]. The nine principal axes, three per well, adhere to the 120° rotational symmetry of the rf electrode, as shown in Fig. 1. In one of these wells, a single $^9Be^+$ ion has motional frequencies $\{\omega_R, \omega_V, \omega_T\} \simeq 2\pi \times \{3.9, 6.9, 10.8\}$ MHz, respectively, along the principal axes, which we name radial (purple), vertical (white), and tangential (gray). The curvatures of all wells are fine-tuned along their radial directions by changing the potentials on the electrodes closest to the ion in the well (shown as purple rectangles in Fig. 1). The motional frequency of radial eigenmode j is connected to its eigenmode curvature by

$$\omega_j = \sqrt{\frac{k_{\mathrm{offs}} + \delta k_j}{m}} \approx \omega_R + \delta\omega_j,$$
$$\omega_R = \sqrt{\frac{k_{\mathrm{offs}}}{m}}, \qquad \delta\omega_j = \frac{\delta k_j}{2m\omega_R}, \tag{2}$$

where, here, m is the mass of a $^9Be^+$ ion. The rate of change of the scaled curvatures with the applied potentials is $\delta s_A/\delta V_A = \delta s_B/\delta V_B \approx 1.2\ \mathrm{mV}^{-1}$. By symmetry, the curvatures in sites B and C change at equal amounts $\alpha\delta s_A/\delta V_A$ with $\alpha \approx -0.383$ and likewise for A and C when δV_B is changed (for more details, see Appendix A).

We apply an approximately 0.5 mT magnetic field to lift the degeneracies in the $^2S_{1/2}$ ground state hyperfine manifold of $^9Be^+$, where the $|{\downarrow}\rangle \equiv |F = 2, m_F = -2\rangle$ and the $|{\uparrow}\rangle \equiv |F = 1, m_F = -1\rangle$ hyperfine states are split by approximately 1.26 GHz. We can drive transitions between all hyperfine ground states by applying a microwave magnetic field resonant with their frequency differences using a half-wave antenna embedded in the ground plane of the trap chip approximately 380 μm away from the trap center [37,38]. An elliptically shaped laser beam with its long axis parallel to the electrode surface and a wavelength of approximately 313 nm illuminates all three ions and is used for Doppler cooling and qubit readout via state-dependent fluorescence on the cycling $|{\downarrow}\rangle \leftrightarrow {}^2P_{3/2}|F = 3, m_F = -3\rangle$ transition [41]. We perform ground state cooling of all motional modes, as well as motional state preparation and analysis of the three ions, using stimulated Raman transitions driven by a pair of counterpropagating, tightly focused 313-nm laser beams detuned approximately 80 GHz from the $^2S_{1/2} \leftrightarrow {}^2P_{1/2}$ transition [41,42]. We achieve an average occupation $\bar{n} < 0.05$ for all nine modes after ground state cooling. Because of the geometry of the vacuum chamber, these Raman beams can illuminate either the ions in sites A and B ("ion A" and "ion B") simultaneously or just a single ion in site C ("ion C").

A helium-gas vibration-isolated closed-cycle cryostat [43] cools the trap and its copper enclosure to approximately 3.5 K, providing cryopumping of residual background gas and reduced ion motional heating rates. Ion lifetimes in the trap are typically many weeks (chiefly limited by user error), and the motional heating rates at this temperature are measured to be approximately $\{\dot{\bar{n}}_{Rj}, \dot{\bar{n}}_{Vj}, \dot{\bar{n}}_{Tj}\} \simeq \{30, 14, 2\}$ phonons/s for the three modes of a single ion confined in any of the three sites ($j \in \{A, B, C\}$), much lower than the interion coupling rates.

IV. STATIC INTERACTION TUNING

When $|s_A|$ and $|s_B|$ are close to zero, the Coulomb interaction couples the radial motion of the ions into three collective normal modes $\mathbf{c}_1$, $\mathbf{c}_2$, and $\mathbf{c}_3$ with scaled curvature eigenvalues δk_1, δk_2, and δk_3 as shown in

Fig. 2(a). We experimentally characterize a cut through the eigenfrequency surfaces along $s_B = 0$ [corresponding to the semitransparent plane in Fig. 2(a)] by tuning the potential δV_A applied to the electrode nearest to site A (see Fig. 1). The Raman beams are aligned with ions in sites A and B, and all modes of motion are cooled to near their ground states. Then, the hyperfine states are optically pumped to ideally prepare $|\downarrow\downarrow\downarrow\rangle_{ABC}|000\rangle_{123}$, where $|lmn\rangle_{123} = |l\rangle_1|m\rangle_2|n\rangle_3$ is a product of number states in the basis of the three coupled radial eigenmodes (note that the coupled 123 basis is distinct from the uncoupled ABC basis).

We then apply a weak oscillating electric field pulse at the ion positions using the chip-integrated antenna (see Refs. [37,38]) and scan its frequency to probe the motional eigenmode frequencies. When the tone is resonant with one of the normal modes, the mode will be excited into a coherent state [44]. We choose the strength and duration of the pulse such that the modes acquire an average motional occupation of $\bar{n}_j \approx 1$. We detect the presence or absence of this motional excitation using a Raman red sideband pulse on both ions followed by fluorescence readout of the ion spin state. The normalized fluorescence of the two ions (which is correlated with the probability that the motion was resonantly excited by the probe electric field) is shown in Fig. 2(b). The bright lines trace the normal mode frequencies in good agreement with the theoretical predictions based on the eigenvalues of Eq. (1) that are shown by colored lines (see Appendix D for details on the fitted lines). We observe the degeneracy of two of the modes at $\delta V_A = 0$ mV expected from the trap symmetry and the predicted gap to the highest mode frequency. The mode eigenvector $\mathbf{c}_1$ remains equal to $1/\sqrt{2}(0,-1,1)$, with δf_1 increasing linearly for $\delta V_A < 0$ and reaching zero where it coalesces with δf_2. For $\delta V_A > 0$, δf_2 continues to increase linearly with the same slope as δf_1 for $\delta V_A < 0$, as expected. Small deviations from the theory are caused by slow drifts in the applied and stray potentials on the order of tens of microvolts that occur on the timescale of hours.

To demonstrate control over the dynamics of a single phonon, ions are trapped in A and C and the Raman beams are moved to only illuminate ion C. With the radial curvatures of the two sites equal, the ions are cooled near their ground state of motion and transferred to the $|\uparrow\rangle$ state with a microwave π pulse. We then drive the approximate transition $|\uparrow\uparrow\rangle_{AC}|00\rangle_{AC} \rightarrow |\uparrow\downarrow\rangle_{AC}|01\rangle_{AC}$ with a Raman sideband π pulse on ion C with a duration of 4 μs. The pulse duration is much shorter than the inverse of the coupling strength between ions, $\Delta\omega_j = \Delta k_j/(2m\omega_R) = 2\pi \times (3.299 \pm 0.002)$ kHz, and, therefore, to a good approximation the phonon is added to ion C before it can transfer appreciably to ion A. The spectral width of the Raman sideband pulse spans the frequencies of both radial eigenmodes, and they therefore can be excited simultaneously by the pulse, creating an entangled state of a single phonon distributed over two eigenmodes [45–47]. By applying another sideband π pulse on ion C at $t \geq 0$, the probability of finding the phonon at ion C is mapped onto the probability $P_\downarrow$ of the ion spin state being $|\downarrow\rangle$, which is detected with state-dependent fluorescence. This probability is shown as a function of the delay t between the sideband pulses in Fig. 3. The single phonon is coherently exchanged hundreds of times. The exchange data have imperfect contrast and a slight asymmetry between the maxima and minima. This is caused by a number of experimental imperfections. A leading cause is residual motional excitation of the ion in site A due to imperfect ground state cooling. This excitation will appear in site C after a complete exchange where $P_\downarrow$ is ideally zero. Because of the finite duration of phonon injection, a small fraction of the population has already transferred to site A when injection ends and will also return to C around the exchange time. This results in a further reduction of maxima and minima of $P_\downarrow$. Imperfect calibration of the injection and extraction pulses, laser amplitude noise, and small fluctuations in stray potentials cause additional loss in contrast. The slight upward trend in the average value of $P_\downarrow$ toward longer evolution time is due to anomalous heating during the free evolution of the system.

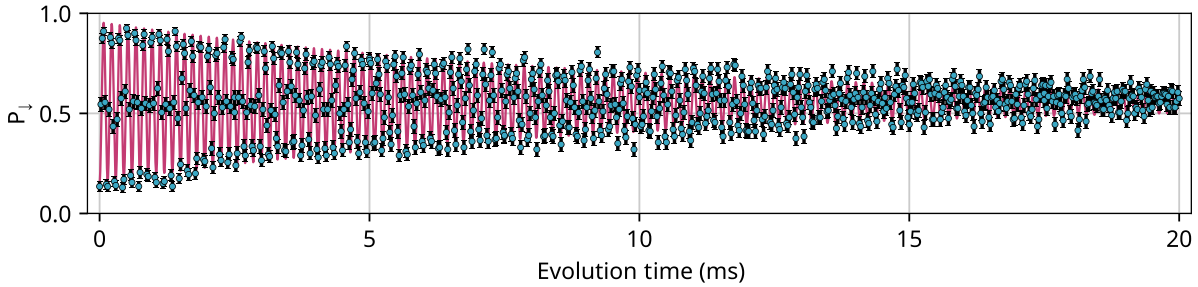


FIG. 3. Probability of finding ion C in $|\downarrow\rangle$ as a function of the evolution time between π pulses that inject and remove a single phonon. With ions in sites A and C and equal site curvatures, a single phonon injected into C is coherently exchanged hundreds of times. Error bars represent 1σ of $P_\downarrow$.

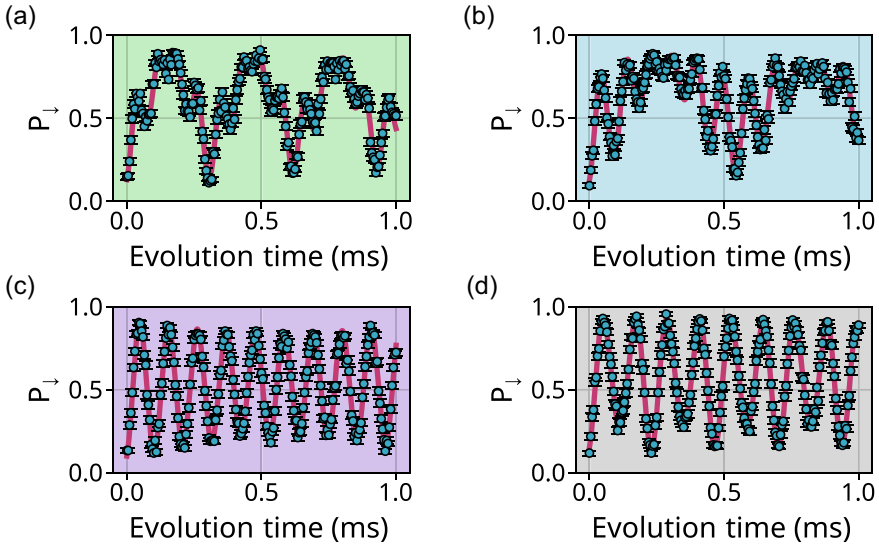


FIG. 4. Single-phonon interference with all three sites occupied and equal radial curvature in sites B and C. (a) $\delta V_A = -1.1$, (b) -0.51, (c) 0.00, and (d) 0.92 mV, respectively. Solid lines are fits to the data. Error bars represent 1σ of $P_\downarrow$.

With ions in all three sites cooled to their ground states of motion and transferred to the $|\uparrow\rangle$ state, we can apply a desired δV_A and inject a phonon into site C as described above. The evolution of the approximate initial motional state $|\psi(0)\rangle = |001\rangle_{ABC}$ can be concisely expressed in the coupled mode basis where the three basis states are energy eigenstates and, therefore, acquire only phases:

$$|\psi(t)\rangle = e^{i\omega_R t}\Big(c_C^{(1)} e^{i\delta\omega_1 t}|100\rangle_{123} + c_C^{(2)} e^{i\delta\omega_2 t}|010\rangle_{123} + c_C^{(3)} e^{i\delta\omega_3 t}|001\rangle_{123}\Big), \tag{3}$$

where the amplitude of the initial state $|001\rangle_{ABC}$ in the kth coupled mode is given by the third eigenvector component $c_C^{(k)}$. For $t > 0$, this evolution periodically delocalizes the phonon over several ions and relocalizes it to ion C (see Appendix B for more details). The second π pulse on the sideband of ion C at $t \geq 0$ maps the probability $P_{001}(t) = |_{ABC}\langle 001|\Psi(t)\rangle|^2$ onto the probability of changing the state of ion C back to $|\uparrow\rangle$. The probability $P_\downarrow = 1 - P_\uparrow = 1 - P_{001}(t)$ is then read out by state-dependent fluorescence. As a function of delay t between the π pulses, $P_{001}(t)$ consists of a sum of up to three sinusoids with amplitudes that depend characteristically on the $c_C^{(k)}$ and oscillate at the differences of the eigenmode frequencies $\delta\omega_k - \delta\omega_l$, $k \neq l$ (see Appendix B). A few examples for different δV_A are shown in Figs. 4(a)–4(d), where a detection of ion C in the bright state $|\downarrow\rangle$ signals that the second π pulse has not flipped the spin state and, therefore, the phonon was not detected in C. A fit to the sum of up to three sinusoids yields the products $|c_C^{(j)}|^2|c_C^{(k)}|^2$ and the frequency differences $\Delta_j = (\delta\omega_j - \delta\omega_1)/(2\pi) = (\delta f_j - \delta f_1)$ for $j \neq 1$. The fitted Δ_j for additional δV_A are overlaid with symbols over the theoretical eigenmode spectrum in Fig. 5 that is plotted using parameters from the independent eigenfrequency determination by weak excitation [see above, Fig. 2(b), and Appendix D for details],

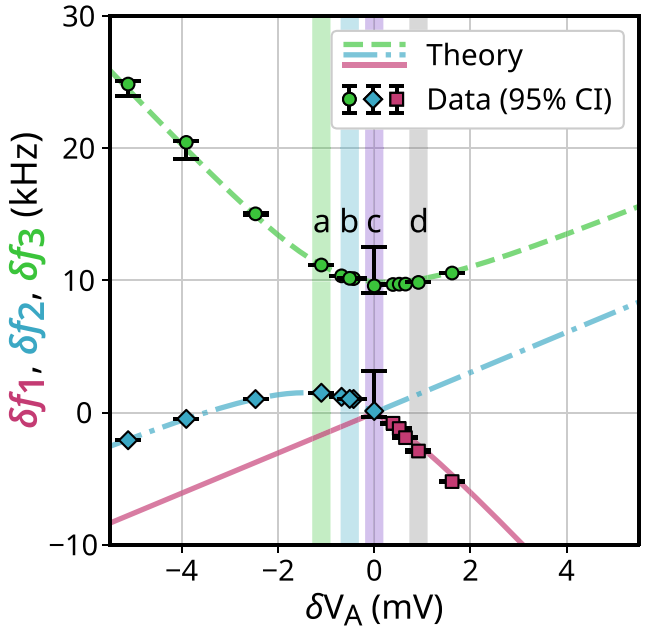


FIG. 5. Frequency differences extracted from single-phonon interference in Figs. 4(a)–4(d), labeled by matching colors, and from additional experiments with different δV_A. The frequency differences are plotted relative to the eigenfrequency that changes linearly with δV_A and are in good agreement with the theoretical eigenmode frequencies for the parameters found from fitting the data in Fig. 2 (solid, dashed, and dash-dotted lines; for details, see Appendix D). Error bars represent 95% confidence intervals obtained from 5000 bootstrapping trials.

showing excellent agreement. This demonstrates that the dynamics of a single phonon can be precisely controlled and behave as expected in the microtrap array. We attribute the imperfect contrast in the exchange data primarily to off-resonant excitation of other transitions due to the relatively large spectral width of the deliberately short sideband π pulses.

V. OBSERVATION OF TOPOLOGICAL BERRY PHASES

At $s_A = s_B = 0$, the lower two eigenmode surfaces [shown in Fig. 2(a) in red and blue] meet at a single point with $\delta k_1 = \delta k_2 = 0$ and form a conical intersection, while points on the highest eigenmode surface (shown in green) have finite values $\delta k_3 \geq 3\Delta k$ for all s_A and s_B. The conical intersection is a topological feature that gives rise to a Berry phase of π for motional states that are prepared on the lower two eigenmode surfaces away from $s_A = s_B = 0$ and then "transported" around the intersection by adiabatic changes $s_A(t)$ and $s_B(t)$ on a closed path $s_{A,B}(t = 0) = s_{A,B}(t = T)$ over the time interval $[0, T]$ [28]. When a state acquires a Berry phase ϕ_{Berry}, this does not change the expectation values of any observable, $\langle\psi|\hat{O}|\psi\rangle = \langle\psi|e^{-i\phi_{\text{Berry}}}\hat{O}e^{i\phi_{\text{Berry}}}|\psi\rangle$, but the phase change can alter the interference between parts of a superposition of states.

The precise controllability of our system enables us to prepare a superposition of states and perform interferometry between them to reveal the Berry phase with high contrast. When setting $s_A(0) = s_B(0) = 1/(\alpha - 1)$ and injecting a single phonon into ion C, this results in the state

$$|\psi(0)\rangle = |001\rangle_{ABC} = \frac{1}{\sqrt{2}}(|010\rangle_{123} + |001\rangle_{123}), \quad (4)$$

an equal amplitude superposition of eigenstates (single-phonon Bell state) on the top two manifolds (see Appendix A for details). Then, $s_{A,B}(t)$ are changed along a path of approximately constant δk_2 ($\delta k_2[s_A(t), s_B(t)] = \delta k_2[s_A(0), s_B(0)]$ for all t), as shown in yellow and pink, respectively, in Figs. 6(a) and 6(b). When the halfway point at $s_A(T/2) = s_B(T/2) = \{[\sqrt{2} - 1 - (\sqrt{2} - 3)\alpha]/(\alpha^2 - 1)\}$ is reached, the path shown in Fig. 6(b) turns around and doubles back on itself, while the path shown in Fig. 6(a) continues on along the mirror image of the first part $[s_{A,B}(t + T/2) = s_{B,A}(t), \quad 0 \leq t \leq T/2]$ and encloses the conical intersection. Because of the symmetry of the system, all eigenvalue surfaces obey $\delta k_j(s_A, s_B) = \delta k_j(s_B, s_A)$, and, therefore, the enclosing and nonenclosing paths pick up equal dynamical phases. The component traveling on the largest eigenvalue surface never encloses a conical intersection and, thus, serves as a reference. After returning to the initial s_A and s_B values at T, the state at $T + t$ with $t > 0$ has evolved to

$$|\psi(T + t)\rangle = \frac{1}{\sqrt{2}}\Big(e^{i(\delta\omega_2 t + \phi_2 + \phi_{\text{Berry}})}|010\rangle_{123} + e^{i(\delta\omega_3 t + \phi_3)}|001\rangle_{123}\Big). \quad (5)$$

Here, ϕ_2 and ϕ_3 are the dynamical phases picked up by the two eigenstates in the superposition on their trajectories (designed to be the same for the encircling and non-encircling paths), and $\phi_{\text{Berry}} = \pi$ is the phase acquired by the $|010\rangle_{123}$ eigenstate from encircling the conical intersection adiabatically; for the path where the intersection was not encircled, $\phi_{\text{Berry}} = 0$. When determining $P_{001}(T + t)$ as in the previously described experiments after traversing the paths in $T = 780$ μs, the Berry phase produces a measured phase shift between the interference fringes shown in Fig. 7 of $\Delta\phi = \pi \times (0.99 \pm 0.01)$, determined by fitting each fringe to a single sinusoid with frequency, phase, and amplitude as free parameters and extracting their phase difference from the fit parameters. We verify the independence of this phase from the shape of

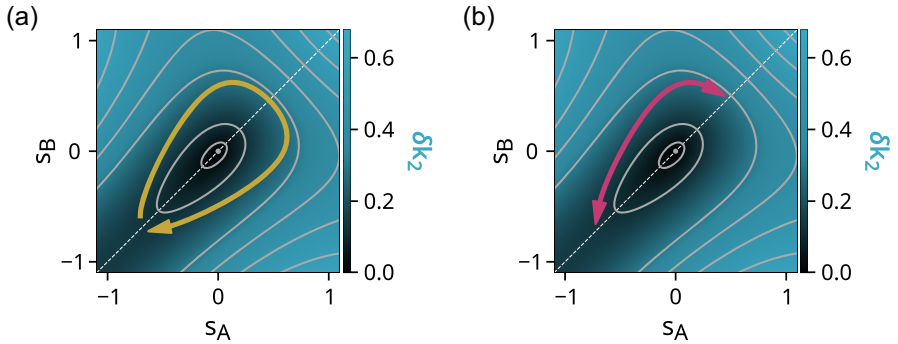


FIG. 6. Paths used in the observation of a topological Berry phase via single-phonon interference. (a) The path on surface δk_2 enclosing the conical intersection as a function of $\{s_A, s_B\}$ and (b) not enclosing the conical intersection. The paths approximate contours of constant curvature (additional equicontours shown in gray). Surface δk_2 is mirror symmetric about the plane indicated by the white dashed line.

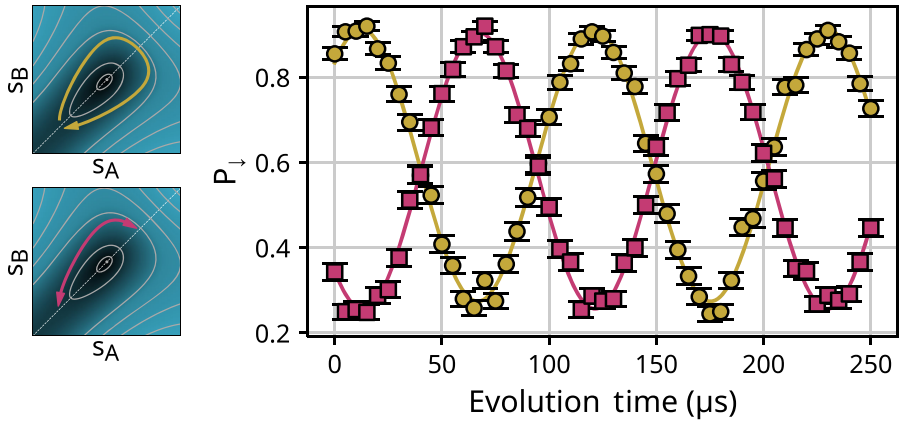


FIG. 7. Observation of a topological Berry phase via single-phonon interference. Observation of $P_\downarrow$ as a function of evolution time after tuning the eigenmodes along an adiabatic, closed path in parameter space that encloses the conical intersection (gold path on the left and gold disks) vs a closed path that does not enclose the intersection (pink path on the left and pink squares). Sinusoidal fits to the data yield a phase difference of $\Delta\phi = \pi \times (0.99 \pm 0.01)$ as expected for the Berry phase acquired on the enclosing path. Solid lines are fits, and error bars represent 1σ of the of $P_\downarrow$.

the path by implementing the same scheme for several other paths that are shown in Figs. 8(a)–8(d) and traversed in 1.8 ms, around their limit for adiabaticity. The different pairs of paths still have equal dynamical phases but surround larger or smaller areas, have more changes of direction, or even connect a number of smaller loops that do not enclose the intersection as the path shown in Fig. 8. Rather than moving along curvature equicontour lines to minimize rates of change as the paths shown in Fig. 6, these paths produce a varying level of nonadiabaticity. This affects the contrast in the interference fringes due to nonadiabatic transitions between different eigenstates and produces slight deviations of the phase difference from the adiabatic value of π. Nevertheless, the acquired phase is largely independent of the shapes of the paths, in accordance with the topological nature of the Berry phase in the fully adiabatic limit.

When reducing the duration T for traversing the pair of paths shown in Figs. 6(a) and 6(b), we observe that the relative phase is reduced from π in the near-adiabatic case, $T \gtrsim 800$ μs to near zero for $T < 200$ μs, as shown by the data points in Fig. 9; the solid green line indicates the phase difference predicted from numerically solving the Schrödinger equation for the enclosing and nonenclosing

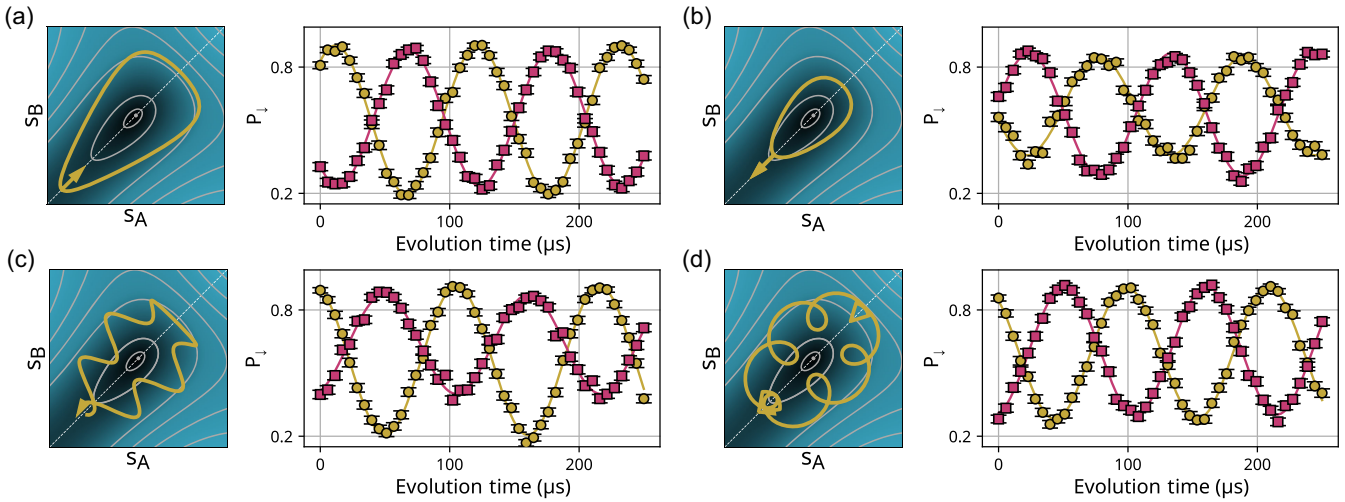


FIG. 8. Topological Berry phases for other paths no longer traversing paths of equal curvature. Only the enclosing paths are shown. The eigenmodes were tuned with a transit duration of $T = 1.8$ ms. (a) Larger area, $\Delta\phi = \pi \times (0.96 \pm 0.02)$. (b) Smaller area, $\Delta\phi = \pi \times (0.97 \pm 0.03)$. (c) Undulating path, $\Delta\phi = \pi \times (1.02 \pm 0.02)$. (d) Multiple additional loops that do not enclose the intersection, $\Delta\phi = \pi \times (0.86 \pm 0.02)$. Solid lines are fits and error bars represent 1σ of of $P_\downarrow$. The deviation from the adiabatic value of $\Delta\phi = \pi$ is likely the result of too rapid changes of $\{s_A, s_B\}$ along the paths.

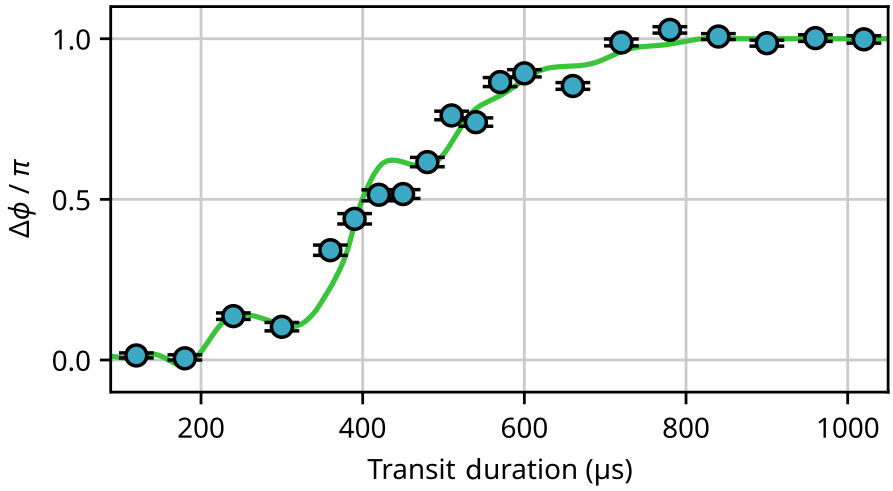


FIG. 9. Observed phase difference when traversing the enclosing and nonenclosing paths with different durations. Data points are shown as blue symbols. The solid line is the phase difference predicted by numerical integration of the Schrödinger equation of the 2D array for the enclosing and nonenclosing paths in parameter space. Error bars are 68% confidence intervals obtained from 5000 bootstrapping trials.

paths. Nonadiabatic evolution also changes the contrast of the interference patterns (not shown), since transitions to the third eigenmode are no longer negligible.

VI. DISCUSSION AND OUTLOOK

In summary, we precisely prepare and control the quantum state of single phonons in coupled harmonic oscillators realized by the Coulomb interaction of three ions in a 2D microtrap array with full control of individual sites. We insert a single phonon into the array, study its behavior for static and dynamical site tuning, and find close agreement with theoretical models of the ideal coupled quantum system. We observe a topological Berry phase by single-phonon interference, demonstrate path independence of the phase in the adiabatic limit, and quantitatively determine the reduction of the phase when adiabaticity of the process is gradually reduced.

The long coherence times and precise control motivate future work with more complex quantum states involving multiple phonons as well as the internal degrees of freedom of the ions, possibly in larger arrays. Desired symmetries in interactions are directly established by the array geometry without requiring additional control fields but can still be combined with the laser fields frequently used to implement potentials and interactions in other atom-based quantum simulators. Array symmetries can subsequently be broken and parameters changed by static or dynamic tuning of the individual local potential wells the ions reside in. Wells can be tuned on timescales slower or faster than the phonon dynamics and studied on all length scales, from a single site to changing or probing domains or properties of the whole array. These capabilities expand the toolkit of prior trapped-ion quantum simulators [15–17,48,49] by directly and intuitively implementing the spatial structures of arbitrary 2D Hamiltonians themselves and adding site-specific degrees of freedom that are both statically and dynamically programmable.

Larger arrays (see Methods in Ref. [26] for example geometries and Ref. [50] for a prototype, four-ion device) require more control electrodes (eight per ion for full control of electric fields and curvatures) and can benefit from integrated optics [51,52] and rf or microwave control [22,53]. The technology required for scaling ion trap systems is a current focus of developments in industry and several national laboratories, where systems with up to 196 ions (98 qubits and 98 helpers) are fully operational [54]. Finite arrays can be used to study topological edge states with single-site resolution or more complex coupled bosonic degrees of freedom [2], including lattice-gauge models [55] and boson sampling [56]. By also incorporating the internal (pseudospin) degrees of freedom of ions, spin-boson models, which have been studied in 1D ion chains [57,58], can be extended to precisely designed 2D geometries with dynamically tunable sites. Effective spin-spin interactions [1,53] can be simulated by driving the array with laser or microwave fields and adiabatically eliminating the ion motion. For example, geometrically frustrated spin models on site-tunable triangular, kagome, and other complex or irregular lattices as well as spin glasses may be realized in this manner. All these systems can be studied with dynamic individual site control and resolution that allows one to introduce disorder or induce phase transitions.

ACKNOWLEDGMENTS

We thank D. T. C. Allcock for the passively stable rf source used in the apparatus, S. Geller for discussions about statistical analysis, Raymond A. Haltli for contributions to

the trap fabrication, and D. Palani and R. Shaniv for reviewing the manuscript. We acknowledge funding from the NIST Quantum Initiative. Authors affiliated with the University of Colorado Boulder were supported by the CU-NIST PREP Program, operated jointly by the University of Colorado Boulder and NIST. Sandia National Laboratories is a multimission laboratory managed and operated by National Technology & Engineering Solutions of Sandia, LLC, a wholly owned subsidiary of Honeywell International Inc., for the U.S. Department of Energy's National Nuclear Security Administration under Contract No. DE-NA0003525.

J. F. N. and D. L. performed the experiments and analyzed the data, with N. K. L. assisting. K. C. M. and J. K. performed preliminary experiments and testing of the ion trap. C. W. H., M. G. B., and E. J. H. led the fabrication of the ion trap. R. S., R. J., and D. L. designed the trap's electrode geometry. S. L. T. and D. H. S., with assistance from R. J., designed and built the cryogenic ion trap system. D. J. W., A. C. W., and D. L. advised the scientific direction of the project during its development and, with D. H. S., secured its funding. D. H. S. provided technical guidance for apparatus and experimental design. J. F. N. and D. L. wrote the manuscript with input from all authors. D. L. supervised the project and developed the theoretical models of the experiments.

The authors declare no competing interests.

This paper describes objective technical results and analysis. Any subjective views or opinions that might be expressed in the paper do not necessarily represent the views of the U.S. Department of Energy or the U.S. Government.

DATA AVAILABILITY

The data that support the findings of this article are not publicly available upon publication because it is not technically feasible and/or the cost of preparing, depositing, and hosting the data would be prohibitive within the terms of this research project. The data are available from the authors upon reasonable request.

APPENDIX A: HESSIAN AND EIGENMODES

With the origin of the coordinate system at the center of an equilateral triangle of trapping sites A, B, and C with mutual distance d_0 (see Fig. 1), the site coordinates are

$$\mathbf{r}_A = \frac{d_0}{2\sqrt{3}}\begin{pmatrix} -\sqrt{3} \\ 1 \\ 0 \end{pmatrix}, \quad \mathbf{r}_B = \frac{d_0}{\sqrt{3}}\begin{pmatrix} 0 \\ -1 \\ 0 \end{pmatrix}, \quad \mathbf{r}_C = \frac{d_0}{2\sqrt{3}}\begin{pmatrix} \sqrt{3} \\ 1 \\ 0 \end{pmatrix}. \tag{A1}$$

We call the principal axes of the rf pseudopotential wells around these sites with the smallest curvature the radial directions. They are tilted by $\theta \approx 19°$ out of the plane of the triangle and oriented as the following unit vectors (shown as purple arrows in Fig. 1, labeled with $\hat{\mathbf{e}}_{RA}$ for site A):

$$\hat{\mathbf{e}}_{RA} = \frac{1}{2}\begin{pmatrix} -\sqrt{3}\cos\theta \\ \cos\theta \\ 2\sin\theta \end{pmatrix}, \qquad \hat{\mathbf{e}}_{RB} = \begin{pmatrix} 0 \\ -\cos\theta \\ \sin\theta \end{pmatrix},$$
$$\hat{\mathbf{e}}_{RC} = \frac{1}{2}\begin{pmatrix} \sqrt{3}\cos\theta \\ \cos\theta \\ 2\sin\theta \end{pmatrix}. \tag{A2}$$

We assume the potential curvature along these radial axes to be identical for each well, with value k_0. Three identical ions with charge q and mass m, one held at each site with equilibrium positions as specified in Eq. (A1), will interact by their mutual Coulomb repulsion. Small displacements $(\delta_A, \delta_B, \delta_C)$ from the equilibrium positions, along the principal axes Eq. (A2) and taken to be much smaller than the ion-ion spacing, change the modulus of the distance between the ions as

$$\begin{aligned} d_{AB} &= |\mathbf{r}_A + \delta_A\hat{\mathbf{e}}_{RA} - \mathbf{r}_B - \delta_B\hat{\mathbf{e}}_{RB}|, \\ d_{BC} &= |\mathbf{r}_B + \delta_B\hat{\mathbf{e}}_{RB} - \mathbf{r}_C - \delta_C\hat{\mathbf{e}}_{RC}|, \\ d_{AC} &= |\mathbf{r}_A + \delta_A\hat{\mathbf{e}}_{RA} - \mathbf{r}_C - \delta_C\hat{\mathbf{e}}_{RC}|. \end{aligned} \tag{A3}$$

Assuming no displacement of the ions from their equilibrium positions normal to the respective axes in Eq. (A2), the potential energy of the Coulomb-coupled system as a function of the small displacements is given by

$$V_0 = \frac{1}{2}k_0(\delta_A^2 + \delta_B^2 + \delta_C^2) + \frac{q^2}{4\pi\epsilon_0}\left(\frac{1}{d_{AB}} + \frac{1}{d_{BC}} + \frac{1}{d_{AC}}\right), \tag{A4}$$

where ϵ_0 is the vacuum permittivity. The Hessian matrix $\mathbf{H}_0$ composed of the second derivatives of V_0 with respect to $(\delta_A, \delta_B, \delta_C)$ with elements $(\mathbf{H}_0)_{ik} = [(\partial^2 V_0)/(\partial\delta_i\partial\delta_k)]$, taken at $\delta_A = \delta_B = \delta_C = 0$, can be rewritten as

$$\begin{aligned} \mathbf{H}_0 &= k_{\text{offs}}\begin{pmatrix} 1 & 0 & 0 \\ 0 & 1 & 0 \\ 0 & 0 & 1 \end{pmatrix} + \Delta k\begin{pmatrix} 1 & 1 & 1 \\ 1 & 1 & 1 \\ 1 & 1 & 1 \end{pmatrix} \\ &\equiv k_{\text{offs}}\mathbf{I} + \Delta k\mathbf{C}, \end{aligned} \tag{A5}$$

with the offset curvature

$$k_{\text{offs}} = k_0 - \frac{q^2}{4\pi\epsilon_0}\frac{9 - 15\cos(2\theta)}{8d_0^3} > 0, \tag{A6}$$

that multiplies the identity matrix $\mathbf{I}$ and is much larger than the prefactor of the coupling matrix $\mathbf{C}$ in our system:

$$\Delta k = \frac{q^2}{4\pi\epsilon_0}\frac{11+3\cos(2\theta)}{8d_0^3} > 0. \tag{A7}$$

Any vector is an eigenvector of the identity matrix, and the coupling matrix $\Delta k\mathbf{C}$ has three identical rows, which implies that it has a null space of dimension two (two nonzero eigenvectors with eigenvalue zero) and a nonzero eigenvalue $3\Delta k$. A certain set of normalized eigenvectors and eigenvalues is

$$\mathbf{c}^{(3)} = \frac{1}{\sqrt{3}}\begin{pmatrix}1\\1\\1\end{pmatrix}, \qquad \mathbf{c}^{(1)} = \frac{1}{\sqrt{2}}\begin{pmatrix}0\\1\\-1\end{pmatrix}, \qquad \mathbf{c}^{(2)} = \frac{1}{\sqrt{6}}\begin{pmatrix}2\\-1\\-1\end{pmatrix}, \tag{A8}$$

$$\delta k_3 = 3\Delta k, \qquad \delta k_1 = 0, \qquad \delta k_2 = 0, \tag{A9}$$

but any linear combination $a\mathbf{c}^{(1)} + b\mathbf{c}^{(2)}$ is also an eigenvector with eigenvalue zero. Another choice of normalized eigenvectors with more obvious threefold symmetry and complex components is

$$\mathbf{c}^{(3)} = \frac{1}{\sqrt{3}}\begin{pmatrix}1\\1\\1\end{pmatrix}, \qquad \mathbf{c}^{(+)} = \frac{1}{\sqrt{3}}\begin{pmatrix}1\\e^{i2\pi/3}\\e^{i4\pi/3}\end{pmatrix}, \qquad \mathbf{c}^{(-)} = \frac{1}{\sqrt{3}}\begin{pmatrix}1\\e^{-i2\pi/3}\\e^{-i4\pi/3}\end{pmatrix}.$$
$$\delta k_3 = 3\Delta k, \qquad \delta k_+ = 0, \qquad \delta k_- = 0. \tag{A10}$$

In this set, exchanging sites leaves $\mathbf{c}^{(3)}$ unchanged. Exchanging sites cyclically (which corresponds to $\pm 2\pi/3$ rotations around the z axis) alters the remaining eigenvectors by a global phase only, and all other permutations transform $\mathbf{c}^{(+)} \leftrightarrow \mathbf{c}^{(-)}$ up to a global phase.

The system can be tuned by applying small potential changes (on the order of 100 μV) that we call "shims" to the electrodes closest to the three ion sites, two of which are shown in purple in Fig. 1. We neglect the very small static electric field at the positions of the ions caused by the shims and consider only the change in the well curvatures. The threefold symmetry dictates that a change of curvature $\Delta k s_A$ in well A due to a potential applied to the electrode closest to site A results in equal changes of well curvature $\alpha\Delta k s_A$ at the two other sites B and C. In our system, $\alpha \approx -0.383$. Moreover, a change of $\{s_A, s_B, s_C\}$ on the electrodes under A, B, and C can be rewritten as a global change of all three electrodes by $k'_{\mathrm{offs}} = k_{\mathrm{offs}} + \Delta k s_C$ and local changes of $\{s_A - s_C, s_B - s_C, 0\}$. Besides the relatively small eigenvalue change from $k_{\mathrm{offs}} \to k'_{\mathrm{offs}}$ with $|\Delta k s_C| \ll k_{\mathrm{offs}}$, the eigenmodes are unaffected by the global change. This renders the shim-parameter space effectively two-dimensional. The space can be explored by just changing potentials under sites A and B which results in curvature changes of $\Delta k\mathbf{S}(s_A, s_B)$ with the unit-free shim matrix

$$\mathbf{S}(s_A, s_B) = \begin{pmatrix} s_A + \alpha s_B & 0 & 0 \\ 0 & s_B + \alpha s_A & 0 \\ 0 & 0 & \alpha(s_A + s_B) \end{pmatrix}. \tag{A11}$$

The curvature changes add to $\mathbf{H}_0$ for the total Hessian matrix:

$$\begin{aligned}\mathbf{H}(s_A, s_B) &= \mathbf{H}_0 + \Delta k\mathbf{S}(s_A, s_B) \\ &= k_{\mathrm{offs}}\mathbf{I} + \Delta k\mathbf{C} + \Delta k\mathbf{S}(s_A, s_B),\end{aligned} \tag{A12}$$

which is identical to Eq. (1) in the main text. The eigenvectors of $\mathbf{H}(s_A, s_B)$ are equal to the eigenvectors of $\mathbf{C} + \mathbf{S}(s_A, s_B)$, and the eigenvalues of $\mathbf{H}(s_A, s_B)$ can be written as $k_j \equiv k_{\mathrm{offs}} + \delta k_j$, with $j = \{0, 1, 2\}$. The general eigensystem with nonzero shims s_A and s_B can be expressed analytically but reduces to simple expressions in only a few special cases.

Because of the threefold symmetry of the unperturbed system, the eigenvalues are identical under exchange of s_A and s_B, $k_j(s_A, s_B) = k_j(s_B, s_A)$. Moreover, when $s_A \neq 0$, $s_B = 0$, wells B and C have equal curvatures that are different from the curvature in well A. The normal mode vector $\mathbf{c}^{(1)} = (1/\sqrt{2})(0, -1, 1)^T$ has no participation from the ion in site A and remains a normal mode vector, irrespective of the value of s_A. The eigenvalue of this

decoupled mode changes linearly as $k = k_{\text{offs}} + \Delta k \alpha s_A$. In analogy for $s_A = 0$, $s_B \neq 0$, there is always a mode with no participation in B. When $s_A = s_B \neq 0$, sites A and B have equal curvatures that are different from the curvature of site C; therefore, one eigenvector has no participation in C. The eigenvalues $\delta k_j(s_A, s_B)$ are shown in Fig. 2(a) as a function of shim parameters $\{s_A, s_B\}$. The eigenvalues form three surfaces that obey the symmetry $\delta k_j(s_A, s_B) = \delta k_j(s_B, s_A)$ and δk_1 and δk_2 have a conical intersection at $\{s_A, s_B\} = \{0, 0\}$ where two eigenvalues are degenerate and equal to zero. The δk_j are ordered by their magnitude $\delta k_1 \leq 0 \leq \delta k_2 < \delta k_3$ and shown in red, blue, and green, respectively.

APPENDIX B: QUANTUM STATES IN THE UNCOUPLED BASIS AND THE EIGENMODE BASIS

We can use basis states of the radial modes composed of products of number states of the three uncoupled harmonic oscillators situated at sites A, B, and C with notation $|klm\rangle_{ABC}$, where the k, l, and m are equal to zero or positive integers. This is a complete basis, and an arbitrary state at time $t = 0$ can be written as

$$|\psi(t=0)\rangle_{ABC} = \sum_{klm} u_{klm} |klm\rangle_{ABC} = \sum_{klm} \frac{u_{klm}}{\sqrt{k!l!m!}} (\hat{a}_A^\dagger)^k (\hat{a}_B^\dagger)^l (\hat{a}_C^\dagger)^m |000\rangle_{ABC}. \tag{B1}$$

In analogy, we denote the products of number states in the coupled radial mode eigenbasis as $|klm\rangle_{123}$. The ground state is identical in any basis: $|000\rangle_{ABC} = |000\rangle_{123}$. When $k_{\text{offs}} \gg \Delta k$, the coupled radial eigenmode frequencies can be related to the curvatures as

$$\omega_j = \sqrt{\frac{k_{\text{offs}} + \delta k_j}{m}} \approx \omega_R + \delta\omega_j, \qquad \omega_R = \sqrt{\frac{k_{\text{offs}}}{m}}, \qquad \delta\omega_j = \frac{\delta k_j}{2m\omega_R}. \tag{B2}$$

The time evolution of the eigenmode creation operators $\hat{a}_j^\dagger$ ($j \in \{1, 2, 3\}$) is particularly simple:

$$\hat{a}_j^\dagger(t) = \hat{a}_j^\dagger(0) e^{i(\omega_R + \delta\omega_j)t}. \tag{B3}$$

The creation operators in the uncoupled basis can be rewritten in terms of the creation operators in the coupled eigenbasis by inserting the eigenmode coordinates of $\mathbf{H}$ in the notation $\mathbf{c}^{(k)} = (c_A^{(k)}, c_B^{(k)}, c_C^{(k)})^T$:

$$\begin{aligned}
\hat{a}_A^\dagger(t) &= e^{i\omega_R t}\left(c_A^{(1)}\hat{a}_1^\dagger(0)e^{i\delta\omega_1 t} + c_A^{(2)}\hat{a}_2^\dagger(0)e^{i\delta\omega_2 t} + c_A^{(3)}\hat{a}_3^\dagger(0)e^{i\delta\omega_3 t}\right),\\
\hat{a}_B^\dagger(t) &= e^{i\omega_R t}\left(c_B^{(1)}\hat{a}_1^\dagger(0)e^{i\delta\omega_1 t} + c_B^{(2)}\hat{a}_2^\dagger(0)e^{i\delta\omega_2 t} + c_B^{(3)}\hat{a}_3^\dagger(0)e^{i\delta\omega_3 t}\right),\\
\hat{a}_C^\dagger(t) &= e^{i\omega_R t}\left(c_C^{(1)}\hat{a}_1^\dagger(0)e^{i\delta\omega_1 t} + c_C^{(2)}\hat{a}_2^\dagger(0)e^{i\delta\omega_2 t} + c_C^{(3)}\hat{a}_3^\dagger(0)e^{i\delta\omega_3 t}\right).
\end{aligned} \tag{B4}$$

This implies that $|\psi(t)\rangle_{ABC}$ written in terms of the coupled eigenbasis creation operators will contain terms that are polynomial in the creation operators:

$$[\hat{a}_A^\dagger(t)]^k |000\rangle_{ABC} = e^{ik\omega_R t}\left[c_A^{(1)}\hat{a}_1^\dagger(0)e^{i\delta\omega_1 t} + c_A^{(2)}\hat{a}_2^\dagger(0)e^{i\delta\omega_2 t} + c_A^{(3)}\hat{a}_3^\dagger(0)e^{i\delta\omega_3 t}\right]^k |000\rangle_{123}. \tag{B5}$$

The sum of all these terms can lead to multipath interference as a function of time, which can give rise to, for example, the complexity in boson sampling [56]. However, all terms in the polynomial will be proportional to $[\hat{a}_1^\dagger(0)]^{k'}[\hat{a}_2^\dagger(0)]^{l'}[\hat{a}_3^\dagger(0)]^{m'}$ where the sum of exponents is preserved $k' + l' + m' = k$. This is also true for the other polynomials with l and m excitations in Eq. (B1), meaning that the total number of excitations in an initial product of number states $|klm\rangle_{ABC}$ is conserved and equal to $k + l + m$ at all times.

The time dependence simplifies for initial states with a single excitation, as the ones prepared in our experiments. In particular, the state $|\psi(0)\rangle = |001\rangle_{ABC}$ evolves to

$$|\psi(t)\rangle = e^{i\omega_R t}\left(c_C^{(1)}e^{i\delta\omega_1 t}|100\rangle_{123} + c_C^{(2)}e^{i\delta\omega_2 t}|010\rangle_{123} + c_C^{(3)}e^{i\delta\omega_3 t}|001\rangle_{123}\right), \tag{B6}$$

the expression stated as Eq. (3) in the main text. The probability P_{001} of finding the phonon in site C at a later time $t > 0$ consists of a constant and up to three oscillating terms at the differences of mode eigenfrequencies:

$$\begin{aligned} P_{001} &= |_{ABC}\langle 001|\Psi(t)\rangle|^2 \\ &= \left|c_C^{(1)}\right|^4 + \left|c_C^{(2)}\right|^4 + \left|c_C^{(3)}\right|^4 \\ &\quad + 2\left|c_C^{(1)}\right|^2\left|c_C^{(2)}\right|^2 \cos[(\delta\omega_2 - \delta\omega_1)t] \\ &\quad + 2\left|c_C^{(1)}\right|^2\left|c_C^{(3)}\right|^2 \cos[(\delta\omega_3 - \delta\omega_1)t] \\ &\quad + 2\left|c_C^{(2)}\right|^2\left|c_C^{(3)}\right|^2 \cos[(\delta\omega_3 - \delta\omega_2)t], \end{aligned} \tag{B7}$$

where certainty is reached whenever all three cosines are equal to one (for example, when $t = 0$); then, $P_{001} = (|c_C^{(1)}|^2 + |c_C^{(2)}|^2 + |c_C^{(3)}|^2)^2 = 1$. If any of the third components $\{c_C^{(1)}, c_C^{(2)}, c_C^{(3)}\}$ of the three coupled basis eigenvectors is equal to zero, or if the frequencies of two eigenmodes are identical $\delta\omega_k = \delta\omega_l$ for $k \neq l$, only one time-dependent term remains.

APPENDIX C: OBSERVING A BERRY PHASE

In the special case where $s_{A0} = s_{B0} = 1/(\alpha - 1)$, the eigensystem becomes

$$\mathbf{c}^{(1)} = \frac{1}{\sqrt{2}}\begin{pmatrix} -1 \\ 1 \\ 0 \end{pmatrix}, \quad \mathbf{c}^{(2)} = \frac{1}{2}\begin{pmatrix} -1 \\ -1 \\ \sqrt{2} \end{pmatrix}, \quad \mathbf{c}^{(3)} = \frac{1}{2}\begin{pmatrix} 1 \\ 1 \\ \sqrt{2} \end{pmatrix},$$
$$\delta k_1 = \Delta k\frac{\alpha+1}{\alpha-1}, \quad \delta k_2 = \Delta k\left(3 - \sqrt{2} + \frac{2}{\alpha-1}\right),$$
$$\delta k_3 = \Delta k\left(3 + \sqrt{2} + \frac{2}{\alpha-1}\right). \tag{C1}$$

The first eigenmode does not participate in site C, while the other two eigenmodes participate equally. When injecting a phonon into site C, the phonon state at $t = 0$ is a single-phonon entangled (Bell) state in the coupled eigenbasis

$$|\psi(0)\rangle = |001\rangle_{ABC} = \frac{1}{\sqrt{2}}(|010\rangle_{123} + |001\rangle_{123}). \tag{C2}$$

The two independent parameters $\{s_A, s_B\}$ that change the external potential curvatures can now be tuned sufficiently slowly compared to $2\pi/|\delta\omega_k - \delta\omega_l|$ for $\{k, l\} \in \{1, 2, 3\}$, $k \neq l$ such that the adiabatic theorem can be applied and the eigenstates of the system approximately remain eigenstates throughout the tuning of $\{s_A, s_B\}$. If a closed path in parameter space is traversed between $t = 0$ and $t = T$, $\{s_A(T), s_B(T)\} = \{s_A(0), s_B(0)\} = \{s_{A0}, s_{B0}\}$, the initial and final eigenstates differ only by a phase and the final state can be written as

$$|\psi(T)\rangle = \frac{1}{\sqrt{2}}(e^{i\phi_2}e^{i\phi_{\text{Berry}}}|010\rangle_{123} + e^{i\phi_3}|001\rangle_{123}), \tag{C3}$$

where

$$\phi_{2,3} = \int_0^T dt'\delta\omega_{2,3}[s_A(t'), s_B(t')] \tag{C4}$$

is the dynamical phase picked up due to the instantaneous frequencies $\delta\omega_{2,3}[s_A(t'), s_B(t')]$ of the eigenmodes 2 and 3 along the path. The dynamical phases are time-dependent generalizations of the dynamical phases $\phi_{2,3} = \delta\omega_{2,3}t$ that appear in Eq. (B6) for s_A and s_B constant in time. In addition, each eigenstate can pick up a Berry phase ϕ_{Berry} that does not depend on details of the path but rather on whether or not the path encloses the conical intersection at $\{s_A, s_B\} = \{0, 0\}$ [28]. The surface $\delta\omega_3(s_A, s_B)$ has no conical intersection, so the component proportional to $|001\rangle_{123}$ will not pick up a Berry phase, irrespective of the path. For the component proportional to $|010\rangle_{123}$, if the intersection is enclosed adiabatically, $\phi_{\text{Berry}} = \pi$; otherwise, $\phi_{\text{Berry}} = 0$.

To isolate the Berry phase, it is advantageous to pick pairs of paths that accumulate the same dynamical phases while one path encloses the conical intersection and the other does not. Because of the symmetry of the eigenvalue surfaces, there is a second point $s_{A1} = s_{B1} = \{[\sqrt{2} - 1 - (\sqrt{2} - 3)\alpha]/(\alpha^2 - 1)\}$ with equal curvature as the initial point, $\delta k_2(s_{A0}, s_{B0}) = \delta k_2(s_{A1}, s_{B1})$ and $\delta k_3(s_{A0}, s_{B0}) = \delta k_3(s_{A1}, s_{B1})$, and these points can be connected by paths of constant curvatures $\delta k_2(s_A, s_B) = \delta k_2(s_{A0}, s_{B0})$ and $\delta k_3(s_A, s_B) = \delta k_3(s_{A0}, s_{B0})$, respectively, as shown in Figs. 6(a) and 6(b). A path that starts at $s_{A0} = s_{B0}$, turns around at $s_{A1} = s_{B1}$, doubles back onto itself, and returns to $s_{A0} = s_{B0}$ will not enclose the conical intersection [Fig. 6(b)]. Since the eigenvalues are identical under exchange of the arguments, $\delta\kappa_j(s_A, s_B) = \delta\kappa_j(s_B, s_A)$, this path will pick up equal dynamical phases as the path that continues clockwise around the intersection shown in Fig. 6(a) and returns to the starting point. Depending on which path is chosen, a Berry phase of zero or π is picked up and the difference will manifest itself as a phase shift of π in the probability $P_{001}(T + t)$ $(t > 0)$ in Eq. (B7) to find the phonon at site C for different delays after either one of the paths has been traversed.

APPENDIX D: FITTING THE DATA IN FIG. 2

A set of 12 data points spanning approximately $\delta f = \pm 2$ kHz around each of the observed resonance peaks in Fig. 2 for fixed δV_A and varying excitation frequency $f_R + \delta f$ was fitted to a Gaussian that yielded the center excitation frequency difference δf_0 and the width of the Gaussian fit. Resonances close to the crossing ($\delta V_A = \{-0.5, 0, 0.5\}$ mV) where two of the peaks are

unresolved in the data were removed, because their convolution produces a single peak with a position that does not easily yield the frequencies of the two underlying resonances. The remaining peak centers approximately form three lines along the light-colored regions in Fig. 2. The model for the eigenmode frequencies is derived from $\mathbf{H}(s_A, s_B)$ by substituting

$$k_{\text{offs}} \to f_R = \frac{1}{2\pi}\sqrt{k_{\text{offs}}/m},$$

$$\Delta k \to \Delta f = \frac{1}{2\pi}\Delta k/(2m\omega_R), \qquad s_A \to c\delta V_A,$$

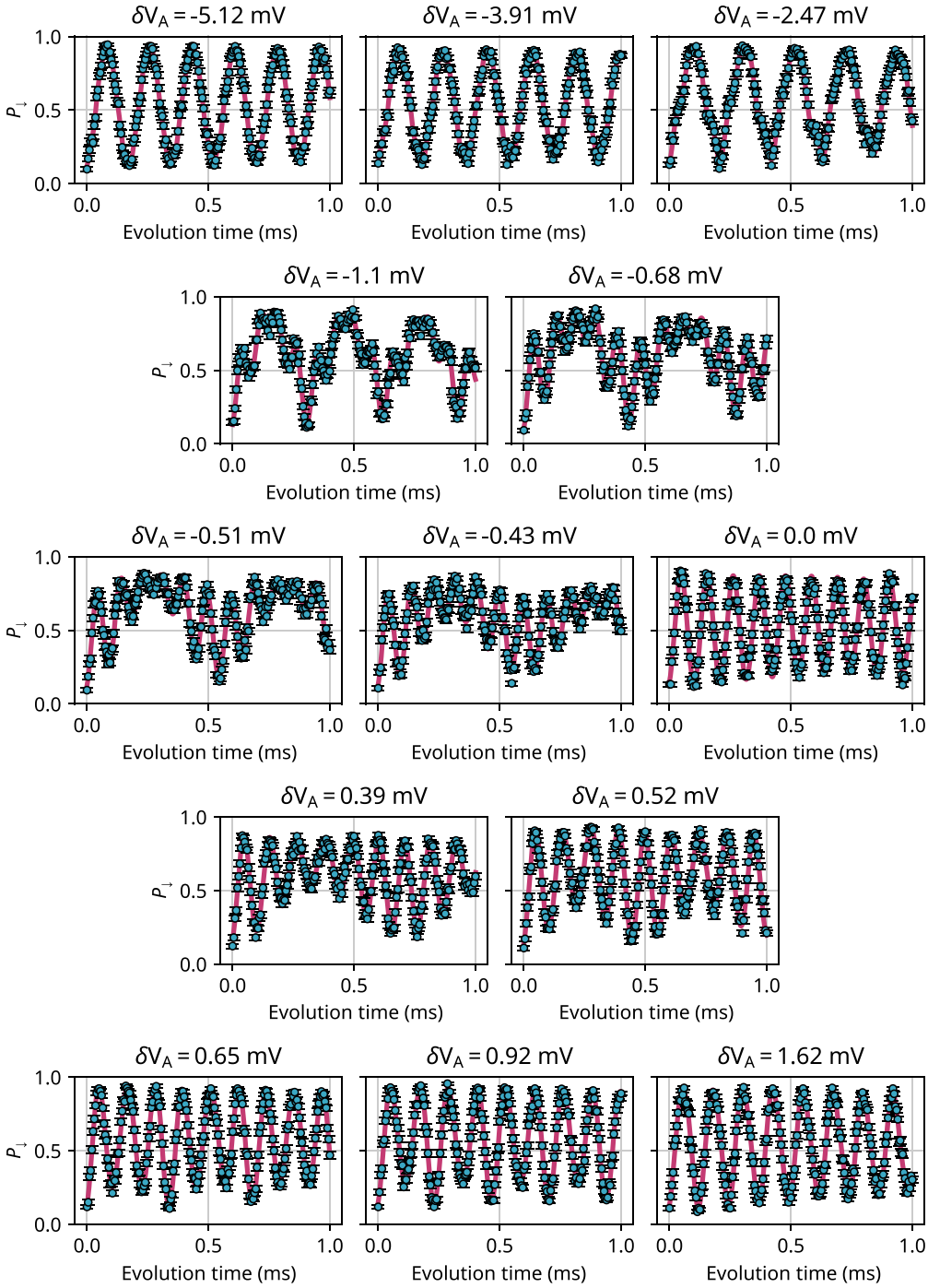


FIG. 10. Single-phonon interferences not shown in Figs. 4(a)–4(d) for the remaining frequency data points as a function of δV_A. As the voltage is changed slightly on the electrode under site A, the observed interference pattern changes. By fitting these data to a sum of sinusoids with different amplitudes (pink lines), the motional frequency differences of the system can be extracted and are shown in Fig. 5. Error bars represent 1σ of $P_\downarrow$.

where c is a constant that has units 1/V and describes the change in the uncoupled site frequency in units of Δf when the shim potential is changed. The matrix

$$\mathbf{F} = f_R \begin{pmatrix} 1 & 0 & 0 \\ 0 & 1 & 0 \\ 0 & 0 & 1 \end{pmatrix} + \Delta f \begin{pmatrix} 1+c\delta V_A & 1 & 1 \\ 1 & 1+\alpha c\delta V_A & 1 \\ 1 & 1 & 1+\alpha c\delta V_A \end{pmatrix} \quad \text{(D1)}$$

derived in this way has the same eigenvectors as the Hessian $\mathbf{H}$ and three eigenvalues:

$$\begin{aligned} f_1 &= f_R + \Delta f \alpha c \delta V_A, \\ f_2 &= f_R + \frac{1}{2}\Delta f(3 + c(1+\alpha)\delta V_A \\ &\quad - \sqrt{9 + 2c(\alpha-1)\delta V_A + c^2(\alpha-1)^2\delta V_A}), \\ f_3 &= f_R + \frac{1}{2}\Delta f(3 + c(1+\alpha)\delta V_A \\ &\quad + \sqrt{9 + 2c(\alpha-1)\delta V_A + c^2(\alpha-1)^2\delta V_A}). \end{aligned} \quad \text{(D2)}$$

Note that the frequency eigenvalues are not expressed and ordered in analogy to the curvature eigenvalue surfaces in the main text. The chosen form shows that f_1 can be directly fit to the set of experimental resonances that vary approximately linearly in δV_A to yield fitted values for $f_R = (3876.60 \pm 0.03)$ kHz (intercept) and $\Delta f \alpha c = (1.52 \pm 0.01)$ kHz/mV (slope). The remaining two resonance frequencies for equal δV_A can be added to each other, and the already determined quantities $2f_R$ and $\Delta f \alpha c \delta V_A$ can be subtracted:

$$f_2 + f_3 - (2f_R + \Delta f \alpha c \delta V_A) = 3\Delta f + \Delta f c \delta V_A,$$

which yields $\Delta f = (3.299 \pm 0.02)$ kHz (intercept) and $\Delta f c = (-3.97 \pm 0.02)$ kHz/mV (slope). The isolated parameters can now be determined: $c = \Delta f c/\Delta f = (-1.202 \pm 0.009)$ 1/mV and $\alpha = \Delta f \alpha c/(\Delta f c) = (-0.383 \pm 0.003)$, where the uncertainties are derived by propagating the uncertainties of the fit parameters through the expressions stated above. By symmetry, c and α also govern the change of frequencies when applying $\delta V_B \neq 0$; $s_B = c\delta V_B$. The frequency eigenvalues as a function of δV_A as determined by the fit are plotted as lines in Figs. 2 and 5 and are in excellent agreement with the data. The fitted function is plotted with all parameters as found from these fits in Fig. 5. The same fit parameters are also used in the theoretical expressions of the bright population in Figs. 4(a)–4(d). Additional fitted phonon exchange results not shown in Figs. 4(a)–4(d) are displayed in Fig. 10. The fitted values are also converted to curvatures according to Eq. (B2) and used in Eq. (1) to compute the intended paths for the Berry phase experiments in Figs. 6(a) and 6(b) and the additional paths shown in Fig. 8.

[1] D. Porras and J. I. Cirac, *Effective quantum spin systems with trapped ions*, Phys. Rev. Lett. **92**, 207901 (2004).

[2] D. Porras and J. I. Cirac, *Bose-Einstein condensation and strong-correlation behavior of phonons in ion traps*, Phys. Rev. Lett. **93**, 263602 (2004).

[3] J. I. Cirac and P. Zoller, *Quantum computations with cold trapped ions*, Phys. Rev. Lett. **74**, 4091 (1995).

[4] S. M. Brewer, J.-S. Chen, A. M. Hankin, E. R. Clements, C. W. Chou, D. J. Wineland, D. B. Hume, and D. R. Leibrandt, $^{27}Al^+$ *quantum-logic clock with a systematic uncertainty below* 10^{-18}, Phys. Rev. Lett. **123**, 033201 (2019).

[5] C.-W. Chou, C. Kurz, D. B. Hume, P. N. Plessow, D. R. Leibrandt, and D. Leibfried, *Preparation and coherent manipulation of pure quantum states of a single molecular ion*, Nature (London) **545**, 203 (2017).

[6] P. Micke, T. Leopold, S. A. King, E. Benkler, L. J. Spieß, L. Schmöger, M. Schwarz, J. R. Crespo López-Urrutia, and P. O. Schmidt, *Coherent laser spectroscopy of highly charged ions using quantum logic*, Nature (London) **578**, 60 (2020).

[7] M. G. Raizen, J. M. Gilligan, J. C. Bergquist, W. M. Itano, and D. J. Wineland, *Ionic crystals in a linear Paul trap*, Phys. Rev. A **45**, 6493 (1992).

[8] F. Diedrich, E. Peik, J. M. Chen, W. Quint, and H. Walther, *Observation of a phase transition of stored laser-cooled ions*, Phys. Rev. Lett. **59**, 2931 (1987).

[9] D. J. Wineland, J. C. Bergquist, W. M. Itano, J. J. Bollinger, and C. H. Manney, *Atomic-ion Coulomb clusters in an ion trap*, Phys. Rev. Lett. **59**, 2935 (1987).

[10] S. L. Gilbert, J. J. Bollinger, and D. J. Wineland, *Shell-structure phase of magnetically confined strongly coupled plasmas*, Phys. Rev. Lett. **60**, 2022 (1988).

[11] Y. Wang, M. Qiao, Z. Cai, K. Zhang, N. Jin, P. Wang, W. Chen, C. Luan, B. Du, H. Wang, Y. Song, D. Yum, and K. Kim, *Coherently manipulated 2D ion crystal in a monolithic Paul trap*, Adv. Quantum Technol. **3**, 2000068 (2020).

[12] M. K. Ivory, A. Kato, A. Hasanzadeh, and B. B. Blinov, *A Paul trap with sectored ring electrodes for experiments with two-dimensional ion crystals*, Rev. Sci. Instrum. **91**, 053201 (2020).

[13] Y. Xie, J. Cui, M. D'Onofrio, A. J. Rasmusson, S. W. Howell, and P. Richerme, *An open-endcap blade trap for radial-2D ion crystals*, Quantum Sci. Technol. **6**, 044009 (2021).

[14] D. Kiesenhofer, H. Hainzer, A. Zhdanov, P. C. Holz, M. Bock, T. Ollikainen, and C. F. Roos, *Controlling two-dimensional Coulomb crystals of more than 100 ions in a monolithic radio-frequency trap*, PRX Quantum **4**, 020317 (2023).

[15] S.-A. Guo, Y.-K. Wu, J. Ye, L. Zhang, W.-Q. Lian, R. Yao, Y. Wang, R.-Y. Yan, Y.-J. Yi, Y.-L. Xu, B.-W. Li, Y.-H. Hou,

Y.-Z. Xu, W.-X. Guo, C. Zhang, B.-X. Qi, Z.-C. Zhou, L. He, and L.-M. Duan, *A site-resolved two-dimensional quantum simulator with hundreds of trapped ions*, Nature (London) **630**, 613 (2024).

[16] J. W. Britton, B. C. Sawyer, A. C. Keith, C.-C. J. Wang, J. K. Freericks, H. Uys, M. J. Biercuk, and J. J. Bollinger, *Engineered two-dimensional Ising interactions in a trapped-ion quantum simulator with hundreds of spins*, Nature (London) **484**, 489 (2012).

[17] J. G. Bohnet, B. C. Sawyer, J. W. Britton, M. L. Wall, A. M. Rey, M. Foss-Feig, and J. J. Bollinger, *Quantum spin dynamics and entanglement generation with hundreds of trapped ions*, Science **352**, 1297 (2016).

[18] J. Zhang, G. Pagano, P. W. Hess, A. Kyprianidis, P. Becker, H. Kaplan, A. V. Gorshkov, Z. X. Gong, and C. Monroe, *Observation of a many-body dynamical phase transition with a 53-qubit quantum simulator*, Nature (London) **551**, 601 (2017).

[19] B.-W. Li, Y.-K. Wu, Q.-X. Mei, R. Yao, W.-Q. Lian, M.-L. Cai, Y. Wang, B.-X. Qi, L. Yao, L. He, Z.-C. Zhou, and L.-M. Duan, *Probing critical behavior of long-range transverse-field Ising model through quantum Kibble-Zurek Mechanism*, PRX Quantum **4**, 010302 (2023).

[20] H. Hainzer, D. Kiesenhofer, T. Ollikainen, M. Bock, F. Kranzl, M. K. Joshi, G. Yoeli, R. Blatt, T. Gefen, and C. F. Roos, *Correlation spectroscopy with multiqubit-enhanced phase estimation*, Phys. Rev. X **14**, 011033 (2024).

[21] A. J. Kollár, M. Fitzpatrick, and A. A. Houck, *Hyperbolic lattices in circuit quantum electrodynamics*, Nature (London) **571**, 45 (2019).

[22] J. Chiaverini and W. E. Lybarger, *Laserless trapped-ion quantum simulations without spontaneous scattering using microtrap arrays*, Phys. Rev. A **77**, 022324 (2008).

[23] R. Schmied, J. H. Wesenberg, and D. Leibfried, *Optimal surface-electrode trap lattices for quantum simulation with trapped ions*, Phys. Rev. Lett. **102**, 233002 (2009).

[24] P. C. Holz, S. Auchter, G. Stocker, M. Valentini, K. Lakhmanskiy, C. Rössler, P. Stampfer, S. Sgouridis, E. Aschauer, Y. Colombe, and R. Blatt, *2D linear trap array for quantum information processing*, Adv. Quantum Technol. **3**, 2000031 (2020).

[25] D. Palani, F. Hasse, P. Kiefer, F. Boeckling, J.-P. Schroeder, U. Warring, and T. Schaetz, *High-fidelity transport of trapped-ion qubits in a multilayer array*, Phys. Rev. A **107**, L050601 (2023).

[26] M. Mielenz, H. Kalis, M. Wittemer, F. Hakelberg, U. Warring, R. Schmied, M. Blain, P. Maunz, D. L. Moehring, D. Leibfried, and T. Schaetz, *Arrays of individually controlled ions suitable for two-dimensional quantum simulations*, Nat. Commun. **7**, ncomms11839 (2016).

[27] F. Hakelberg, P. Kiefer, M. Wittemer, U. Warring, and T. Schaetz, *Interference in a prototype of a two-dimensional ion trap array quantum simulator*, Phys. Rev. Lett. **123**, 100504 (2019).

[28] M. V. Berry, *Quantal phase factors accompanying adiabatic changes*, Proc. R. Soc. A **392**, 45 (1984).

[29] J. Larson, E. Sjöqvist, and P. Öhberg, *Conical Intersections in Physics* (Springer, New York, 2020).

[30] A. H. Castro Neto, F. Guinea, N. M. R. Peres, K. S. Novoselov, and A. K. Geim, *The electronic properties of graphene*, Rev. Mod. Phys. **81**, 109 (2009).

[31] W. Domcke and D. R. Yarkony, *Role of conical intersections in molecular spectroscopy and photoinduced chemical dynamics*, Annu. Rev. Phys. Chem. **63**, 325 (2012).

[32] A. K. Geim and K. S. Novoselov, *The rise of graphene*, Nat. Mater. **6**, 183 (2007).

[33] L. Duca, T. Li, M. Reitter, I. Bloch, M. Schleier-Smith, and U. Schneider, *An Aharonov-Bohm interferometer for determining Bloch band topology*, Science **347**, 288 (2015).

[34] C. S. Wang, N. E. Frattini, B. J. Chapman, S. Puri, S. M. Girvin, M. H. Devoret, and R. J. Schoelkopf, *Observation of wave-packet branching through an engineered conical intersection*, Phys. Rev. X **13**, 011008 (2023).

[35] C. H. Valahu, V. C. Olaya-Agudelo, R. J. MacDonell, T. Navickas, A. D. Rao, M. J. Millican, J. B. Pérez-Sánchez, J. Yuen-Zhou, M. J. Biercuk, C. Hempel, T. R. Tan, and I. Kassal, *Direct observation of geometric-phase interference in dynamics around a conical intersection*, Nat. Chem. **15**, 1503 (2023).

[36] J. Whitlow, Z. Jia, Y. Wang, C. Fang, J. Kim, and K. R. Brown, *Quantum simulation of conical intersections using trapped ions*, Nat. Chem. **15**, 1509 (2023).

[37] N. K. Lysne, J. F. Niedermeyer, A. C. Wilson, D. H. Slichter, and D. Leibfried, *Individual addressing and state readout of trapped ions utilizing radio-frequency micromotion*, Phys. Rev. Lett. **133**, 033201 (2024).

[38] J. F. Niedermeyer, *Quantum control in a two-dimensional ion microtrap array*, Ph.D. thesis, University of Colorado Boulder, Colorado, United States, 2025.

[39] P. L. W. Maunz, *High Optical Access Trap 2.0.*, Technical Report, SAND-2016-0796R (Sandia National Lab. (SNL-NM), Albuquerque, NM (United States), 2016).

[40] D. J. Berkeland, J. D. Miller, J. C. Bergquist, W. M. Itano, and D. J. Wineland, *Minimization of ion micromotion in a Paul trap*, J. Appl. Phys. **15**, 5025 (1998).

[41] D. J. Wineland, C. Monroe, W. M. Itano, D. G. Leibfried, B. E. King, and D. M. Meekhof, *Experimental issues in coherent quantum-state manipulation of trapped atomic ions*, J. Res. Natl. Inst. Stand. Technol. **103**, 259 (1998).

[42] C. Monroe, D. M. Meekhof, B. E. King, S. R. Jefferts, W. M. Itano, D. J. Wineland, and P. Gould, *Resolved-sideband Raman cooling of a bound atom to the 3D zero-point energy*, Phys. Rev. Lett. **75**, 4011 (1995).

[43] S. L. Todaro, *Scalable state detection and fast transport of trapped-ion qubits for quantum computing*, Ph.D. thesis, University of Colorado Boulder, Colorado, United States, 2020.

[44] K. C. McCormick, J. Keller, D. J. Wineland, A. C. Wilson, and D. Leibfried, *Coherently displaced oscillator quantum states of a single trapped atom*, Quantum Sci. Technol. **4**, 024010 (2019).

[45] K. R. Brown, C. Ospelkaus, Y. Colombe, A. C. Wilson, D. Leibfried, and D. J. Wineland, *Coupled quantized mechanical oscillators*, Nature (London) **471**, 196 (2011).

[46] M. Harlander, R. Lechner, M. Brownnutt, R. Blatt, and W. Hänsel, *Trapped-ion antennae for the transmission of quantum information*, Nature (London) **471**, 200 (2011).

[47] A. C. Wilson, Y. Colombe, K. R. Brown, E. Knill, D. Leibfried, and D. J. Wineland, *Tunable spin–spin interactions and entanglement of ions in separate potential wells*, Nature (London) **512**, 57 (2014).

[48] M. Qiao, Z. Cai, Y. Wang, B. Du, N. Jin, W. Chen, P. Wang, C. Luan, E. Gao, X. Sun, H. Tian, J. Zhang, and K. Kim, *Tunable quantum simulation of spin models with a two-dimensional ion crystal*, Nat. Phys. **20**, 623 (2024).

[49] M. Foss-Feig, G. Pagano, A. C. Potter, and N. Y. Yao, *Progress in trapped-ion quantum simulation*, Annu. Rev. Condens. Matter Phys. **16**, 145 (2025).

[50] U. Warring, F. Hakelberg, P. Kiefer, M. Wittemer, and T. Schaetz, *Trapped ion architecture for multi-dimensional quantum simulations*, Adv. Quantum Technol. **3**, 1900137 (2020).

[51] K. K. Mehta, C. Zhang, M. Malinowski, T.-L. Nguyen, M. Stadler, and J. P. Home, *Integrated optical multi-ion quantum logic*, Nature (London) **586**, 533 (2020).

[52] R. J. Niffenegger, J. Stuart, C. Sorace-Agaskar, D. Kharas, S. Bramhavar, C. D. Bruzewicz, W. Loh, R. T. Maxson, R. McConnell, D. Reens, G. N. West, J. M. Sage, and J. Chiaverini, *Integrated multi-wavelength control of an ion qubit*, Nature (London) **586**, 538 (2020).

[53] R. Schmied, J. H. Wesenberg, and D. Leibfried, *Quantum simulation of the hexagonal Kitaev model with trapped ions*, New J. Phys. **13**, 115011 (2011).

[54] A. Ransford *et al.*, *A 98-qubit trapped-ion quantum computer with all-to-all connectivity*, Nature (London) **655**, 81 (2026).

[55] A. Bermudez, T. Schaetz, and D. Porras, *Synthetic gauge fields for vibrational excitations of trapped ions*, Phys. Rev. Lett. **107**, 150501 (2011).

[56] S. Aaronson and A. Arkhipov, *The computational complexity of linear optics*, Theory Comput. **9**, 143 (2013).

[57] Q.-X. Mei, B.-W. Li, Y.-K. Wu, M.-L. Cai, Y. Wang, L. Yao, Z.-C. Zhou, and L.-M. Duan, *Experimental realization of the Rabi-Hubbard model with trapped ions*, Phys. Rev. Lett. **128**, 160504 (2022).

[58] B.-W. Li, Q.-X. Mei, K. Wu, M.-L. Cai, Y. Wang, L. Yao, Z.-C. Zhou, and L.-M. Duan, *Observation of non-Markovian spin dynamics in a Jaynes-Cummings-Hubbard model using a trapped-ion quantum simulator*, Phys. Rev. Lett. **129**, 140501 (2022).